Title
Ligand-Free Processable Perovskite Semiconductor Ink

Journal
Nano Letters, 21(20)

ISSN
1530-6984

Authors
Folgueras, Maria C
Louisia, Sheena
Jin, Jianbo
et al.

Publication Date
2021-10-27

DOI
10.1021/acs.nanolett.1c03308

Peer reviewed

Ligand-free processable perovskite semiconductor ink

Maria C. Folgueras[1,4], Sheena Louisia[2,3], Jianbo Jin[2,4], Mengyu Gao[1,7], Alexandra Du[2], Sirine C. Fakra[5], Rui Zhang[4], Fabian Seeler[6], Kerstin Schierle-Arndt[4,6], and Peidong Yang[1,2,4,7,8]*

1 Department of Materials Science and Engineering, University of California, Berkeley, Berkeley, California 94720, United States.

2 Department of Chemistry, University of California, Berkeley, Berkeley, California 94720, United States.

3 Chemical Sciences Division, Lawrence Berkeley National Laboratory, Berkeley, California 94720, United States.

4 California Research Alliance (CARA), BASF Corporation, Berkeley, California 94720, United States.

5 Advanced Light Source, Lawrence Berkeley National Laboratory, Berkeley, California 94720, United States.

6 BASF SE, Ludwigshafen am Rhein 67056, Germany.

7 Materials Sciences Division, Lawrence Berkeley National Laboratory, Berkeley, California 94720, United States.

8 Kavli Energy NanoScience Institute, Berkeley, California 94720, United States.

* Email: p_yang@berkeley.edu

KEYWORDS: octahedral building block, ligand-free semiconductor ink, building block assembly, ionic octahedron network (ION), halide perovskites

ABSTRACT

Traditional covalent semiconductors require complex processing methods for device fabrication due to their high cohesive energies. Here, we develop a stable, ligand-free perovskite semiconductor ink that can be used to make patterned semiconductor-based optoelectronics in one step. The perovskite ink is formed via the dissolution of crystals of vacancy-ordered double perovskite Cs_2TeX_6 ($X = Cl^-, Br^-, I^-$) in polar aprotic solvents, leading to the stabilization of isolated $[TeX_6]^{2-}$ octahedral anions and free Cs^+ cations without the presence of ligands. The stabilization of the fundamental perovskite ionic octahedral building blocks in solution creates multi-functional inks with the ability to reversibly transform between the liquid ink and the solid-state perovskite crystalline system in air within minutes. These easily processable inks can be patterned onto various materials via dropcasting, stamping, and spraying or painting, highlighting the crucial role of solvated octahedral complexes towards rapid formation of phase-pure perovskite structures in ambient conditions.

TEXT

Traditional covalent semiconductors such as silicon (Si), germanium (Ge), and gallium arsenide (GaAs) are widely used in the semiconductor industry due to their excellent material properties such as desirable exciton binding energies, tunable carrier concentrations, and high carrier mobilities. On top of this, the high cohesive energy associated with the strong covalent bonding in these materials[1] imbue high stability and long operating lifetimes,[2] thus making them ideal candidates for applications in microelectronics,[3] photovoltaics,[4] lasers,[5] etc. However, the bonding nature of these covalent semiconductors inevitably make them energy-intensive to process for device fabrication, requiring very complex, high-temperature, and costly synthetic methods.[6–8] As such, these covalent semiconductors typically are not solution processable except in some cases using colloidal quantum dots.[9,10] These covalent solids cannot be readily disassembled into fundamental building blocks via simply dissociating the bulk solid-phase semiconductor or precursors in solvents, and then cannot be re-assembled back into the solid state without intensive energy input.

On the other hand, organic electronics typically involve solvent-processable polymers and/or macromolecules that are readily patternable and printable but require inert atmosphere or high vacuum processing environments.[11–13] Here we demonstrate that such solution processability of an inorganic semiconductor can be achieved much more easily from an ionic crystal structure, where individual ionic building blocks are directly used as the processable units. In particular, ABX_3 halide perovskites such as $CsPbX_3$ and $CsSnX_3$ ($X = Cl^-$, Br^-, I^-) have recently garnered much interest as such a processable semiconductor system. Their soft ionic lattices allow for ease of fabrication and result in excellent optoelectronic properties,[14,15] making these materials viable options for applications in photovoltaics,[16,17] light-emitting diodes,[18–20] and

photodetectors.[21] The combination of high defect tolerance and low-cost solution processability has made them an attractive candidate for controlled patterning of devices, which could revolutionize the optoelectronics and flexible electronics industries.[22,23] Various studies have highlighted the development or use of solution-phase perovskites with varying stabilized building block units (i.e., quantum dots, solvated precursors, etc.), and how these inks can be deposited onto a substrate to fabricate semiconductor devices.[22,24–29] However, true perovskite inks with stabilized A-site cations and $[BX_6]$ octahedral building blocks have yet to be achieved. Furthermore, achieving high-quality solution processing in ambient conditions is challenging for many of the traditional perovskite systems due to their environmental instability, primarily against moisture and oxygen.[30,31] To achieve a truly facile patterning process, the perovskite semiconductor solutions need to be stable while allowing for rapid phase-pure perovskite formation in ambient conditions. Furthermore, the stability of these solutions should be achieved without the need for passivation, particularly through the means of ligands, as this would ultimately affect the resulting device performance.[32]

We have designed a ligand-free, zero-dimensional (0D) perovskite semiconductor ink that can be easily converted within minutes in ambient conditions to its phase-pure crystalline solid-phase perovskite upon application to and drying on various substrates. These inks of vacancy-ordered double perovskite Cs_2TeX_6 ($X = Cl^-$, Br^-, I^-) can be stabilized in the polar aprotic solvents dimethyl sulfoxide (DMSO) and *N,N*-dimethylformamide (DMF) from bulk Cs_2TeX_6 semiconductor powders and remain stable for at least 1 year. In effect, the polar aprotic solvents serve to disassemble the extended perovskite ionic octahedron network (ION)[33] of the Cs_2TeX_6 bulk powders into its constituent ionic building blocks. The units stabilized in the pure-halide Cs_2TeX_6 inks are Cs^+ cations and $[TeX_{6-n}]^{(2-n)-}$ ($n = 0,1,2$) complex anions, with the anion

population favoring a majority of $[TeX_6]^{2-}$ octahedral complex anions at higher concentrations. The stabilized complexes are critical to the ability of these inks to rapidly form phase-pure perovskite structures in ambient conditions. The formation of thin films, patterns, and dried paints (i.e., coatings) via dropcasting, stamping, and spraying or painting, respectively, with these inks represents the facile reassembly of the solid-phase perovskite crystals directly from the liquid-phase perovskite ink in one simple step.

By using an anti-solvent such as methanol or acetonitrile, phase-pure Cs_2TeCl_6, Cs_2TeBr_6, and Cs_2TeI_6 microcrystals can be formed from the starting precursors with nearly 100% yield (Figure S1). The pure-halide inks Cs_2TeCl_6, Cs_2TeBr_6, and Cs_2TeI_6 are formed simply by dissolving these respective pure-halide powders into their cationic and anionic species in the polar aprotic solvents DMSO or DMF. The mixed-halide inks representing the alloy spaces of $Cs_2TeCl_{6-x}Br_x$ and $Cs_2TeBr_{6-x}I_x$ (x = 0-6) are designed from the appropriate ratio of pure-halide powders. For example, to form an ink of composition $Cs_2TeCl_3Br_3$, a 1:1 molar ratio of Cs_2TeCl_6:Cs_2TeBr_6 powders must be used. The same ink formation behavior is achieved when dissolving Cs_2TeX_6 single crystals in either DMSO or DMF, or when dissolving the stoichiometric amount of respective Cs_2TeX_6 precursors (2CsX and TeX_4) in either DMSO or DMF. The formation of mixed-halide inks creates a tunable solution-phase composition space from bright yellow to deep orange in $Cs_2TeCl_{6-x}Br_x$ (x = 0-6) inks, and from deep orange to black in $Cs_2TeBr_{6-x}I_x$ (x = 0-6) inks (Figure 1a). Starting from the bulk Cs_2TeX_6 semiconductor crystals, we obtain a tunable Cs_2TeX_6 semiconductor ink composition space that forms through the dissociation of the extended Cs_2TeX_6 ionic crystals into their constituent ions, namely solvated Cs^+ cations and $[TeX_6]^{2-}$ octahedral complex anions (Figure 1b). Through this simple design, we can control the unique structural flexibility of halide perovskite lattices by (1)

forming solid-state Cs_2TeX_6 perovskite from solution via an anti-solvent and (2) forming liquid-phase Cs_2TeX_6 perovskite from the bulk solid by using a solvent.

UV-visible absorption spectroscopy measurements suggest the presence of these solvated $[TeX_6]^{2-}$ octahedral complex anions stabilized within the inks (Figure 1c). These spectra reveal absorbance bands associated with the $^1S_0 \rightarrow {}^3P_1$, $^1S_0 \rightarrow {}^3P_2$, and $^1S_0 \rightarrow {}^1P_1$ transitions (generally known as the A, B, and C absorbance bands, respectively) expected from molecular octahedral $[TeX_6]^{2-}$ complexes.[34–36] When changing from $[TeCl_6]^{2-}$ to $[TeBr_6]^{2-}$ to $[TeI_6]^{2-}$ molecular complexes, the molecular energy levels shift corresponding to the different molecular orbital wavefunctions involved, such that the absorption onset red-shifts. These spectra also have strong absorbance features in the UV range, which potentially correspond to undercoordinated Te-based complexes (i.e., $[TeX_4]$ and $[TeX_5]^{1-}$). Given the solution-phase nature of this system, it is likely that there is an equilibrium reaction of $[TeX_6]^{2-} \rightleftharpoons [TeX_{6-n}]^{(2-n)-} + nX^-$ (n = 1,2) occurring within the inks at room temperature.[35] Additionally, the tunable nature of the $Cs_2TeCl_{6-x}Br_x$ and $Cs_2TeBr_{6-x}I_x$ (x = 0-6) inks is observed through progressive shifting of the absorption onset to higher wavelengths, with the expected molecular octahedral complexes being observed in the absorption spectra (Figure S2). All inks maintain their vibrant colors and molecular octahedral absorbance features after 1 year in ambient conditions (20–22°C, relative humidity (RH) = 50–55%), highlighting the exceptional stability of these inks (Figure S3 and Figure S4).

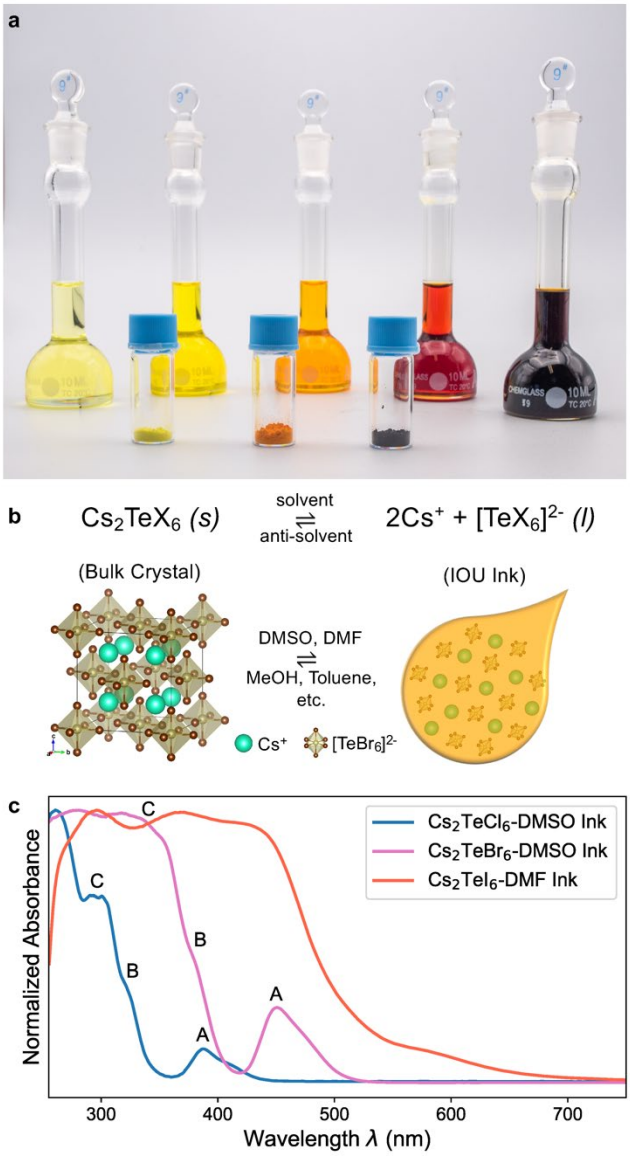

Figure 1. Tunability of the ligand-free 0D Cs_2TeX_6 inks. (a) The Cs_2TeCl_6, $Cs_2TeCl_3Br_3$, Cs_2TeBr_6, $Cs_2TeBr_3I_3$, and Cs_2TeI_6 inks with the respective bulk Cs_2TeCl_6, Cs_2TeBr_6, and Cs_2TeI_6 powders used to fabricate them. Color tunability from bright yellow (Cs_2TeCl_6-DMSO) to deep orange (Cs_2TeBr_6-DMSO) to black (Cs_2TeI_6-DMF) is observed across the inks. (b) Schematic representation of the reversible reaction between the solid-state Cs_2TeX_6 bulk semiconductor and the liquid-phase Cs_2TeX_6 ionic octahedral unit (IOU) ink. The IOU ink is achieved by dissociating the bulk semiconductor in solvents such as DMSO or DMF, and the bulk semiconductor is

reprecipitated by combining the IOU ink with an anti-solvent such as methanol, toluene, etc. (c) Absorption spectra of the Cs_2TeCl_6-DMSO, Cs_2TeBr_6-DMSO, and Cs_2TeI_6-DMF inks. The characteristic absorbance features of molecular octahedral complexes (A, B, and C bands) are indicated for the Cs_2TeCl_6 and Cs_2TeBr_6 inks.

High quality crystalline thin films can be produced directly from the inks via dropcasting onto glass or Si substrates (Figure 2a), representing the re-assembly of Cs_2TeX_6 crystals from the solution-phase. The solution-phase transforms in one minute into the Cs_2TeX_6 thin film with the assistance of heat and an anti-solvent to accelerate solvent evaporation and to improve film coverage and morphology, respectively.[37,38] This effectively closes the loop to our design of reversible ionic building block assembly, whereby the solid-state Cs_2TeX_6 perovskite crystals are re-formed from the liquid-phase perovskite ink by using an anti-solvent. These thin films possess tunable color like their powder counterparts, from bright yellow for Cs_2TeCl_6 to bright orange for Cs_2TeBr_6 to black for Cs_2TeI_6. The Cs_2TeCl_6 thin film maintains the strong yellow emission (λ_{em} = 588 nm) with a photoluminescence quantum yield (PLQY) of 2.06% that is observed in its powder counterpart (Figure 2b,c), and the Cs_2TeBr_6 thin film maintains the red emission (λ_{em} = 670 nm) observed in its powder counterpart (Figure S5). The broad emission of these films is indicative of self-trapped exciton (STE) emission behavior, which in isolated octahedral perovskite systems occurs by the excitation of STEs (i.e., localized Frenkel excitons) and their subsequent recombination through the transition $^3P_{0,1,2} \rightarrow {}^1S_0$ (Table S1).[39–41] All thin films result in good coverage of the substrate, relatively uniform micro-grain morphology (Figure S6), and excellent structural and luminescent stability in ambient conditions (Figure S7).

In addition to their use in thin film formation, these inks can also be used in patterning applications, either by spraying or painting on synthetic fibers, or by stamping on rice (Xuan) paper. Microcrystalline dried paints (i.e., coatings) can be produced from the inks by using either a spray airbrush or a paint brush on synthetic fibers such as cellulose wipes (Figure 2d). The semiconductor ink transforms within minutes into the solid-phase Cs_2TeX_6 semiconductor coating with the assistance of heat. The formation of coatings as Cs_2TeX_6 microcrystals on the synthetic fibers (Figure S3) represents another route towards re-assembly of the Cs_2TeX_6 semiconductor from the solution-phase. These coatings possess tunable color like their powder counterparts, and the Cs_2TeCl_6 coating maintains the strong yellow emission (λ_{em} = 588 nm, PLQY = 2.06%) observed in its powder counterpart (Figure 2e). Similarly, patterned Cs_2TeX_6 microcrystals can be achieved by coating stamps with the inks and pressing onto heated rice paper (Figure 2f). The solution-phase transforms into the solid-state Cs_2TeX_6 semiconductor within a minute without spreading along the paper, thus achieving Cs_2TeX_6 perovskite patterning through stamping (a form of printing). These patterning results indicate that inkjet printing of these Cs_2TeX_6 inks is likely possible, which is currently being investigated.

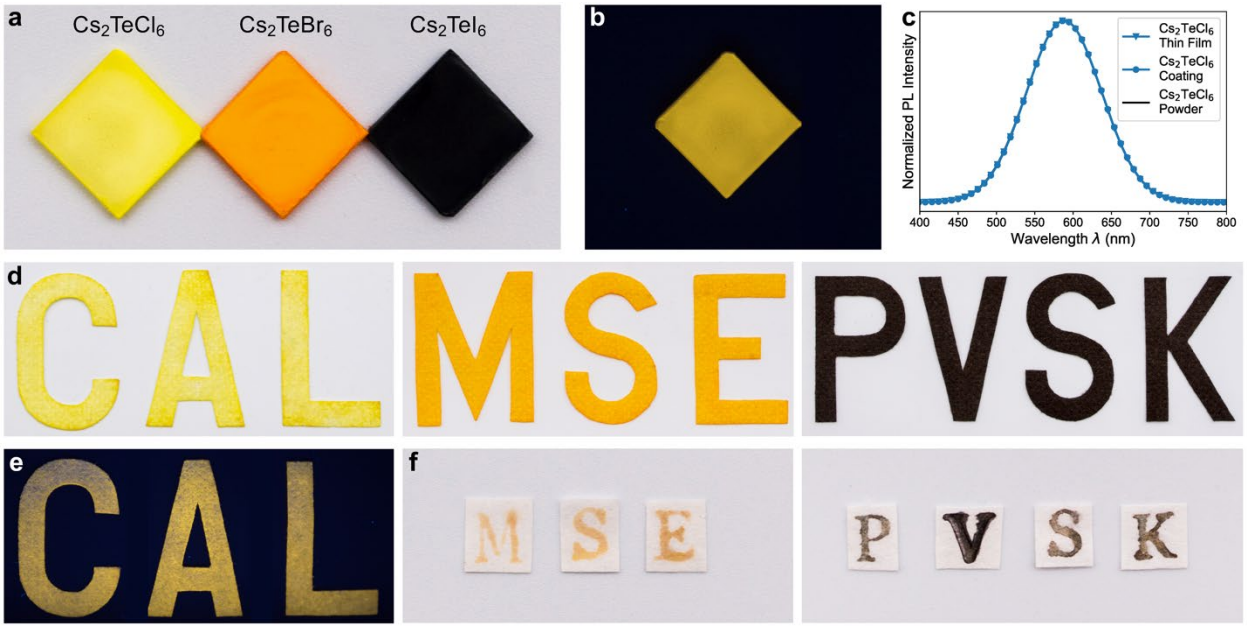

Figure 2. Examples of applications of the inks. (a) Thin films produced by dropcasting Cs_2TeCl_6-DMSO, Cs_2TeBr_6-DMSO, and Cs_2TeI_6-DMF inks, respectively, onto a heated glass substrate with an anti-solvent. (b) Strong yellow emission from a Cs_2TeCl_6 thin film under UV excitation (λ_{ex} = 302 nm). (c) Photoluminescence spectra of a Cs_2TeCl_6 thin film and Cs_2TeCl_6 coating compared with that of the respective Cs_2TeCl_6 powder. (d) Coatings produced by spraying Cs_2TeCl_6-DMSO, Cs_2TeBr_6-DMSO, and Cs_2TeI_6-DMF inks, respectively, onto laboratory cellulose wipes and drying with heat. The same results are achieved via painting the inks onto the wipes. (e) Strong yellow emission from a Cs_2TeCl_6 coating under UV excitation (λ_{ex} = 302 nm). (f) Patterning achieving by stamping Cs_2TeBr_6-DMSO and Cs_2TeI_6-DMF inks, respectively, onto heated rice paper.

The formation of Cs_2TeCl_6, Cs_2TeBr_6, and Cs_2TeI_6 thin films and patterned coatings is confirmed. The thin films and coatings of all three pure-halide compositions have a face-centered cubic (FCC) crystal structure with a tunable lattice parameter from 10.46 Å for Cs_2TeCl_6 to

10.92 Å for Cs_2TeBr_6 to 11.68 Å for Cs_2TeI_6, matching with the lattice parameters of the respective Cs_2TeX_6 powders (Figure S8). The Raman spectra of these thin films and coatings show three fundamental modes that are representative of the expected O_h symmetry of these compositions (Figure S9). These same three fundamental modes are present in the Raman spectra of the corresponding powders. The absorption spectra of the pure-halide thin films show the same behavior as that of the powders, with the absorption onset remaining constant between the respective compositions in thin film or powder forms (Figure S10). As proof of concept, a representative mixed-halide composition $Cs_2TeCl_3Br_3$ thin film is made from the $Cs_2TeCl_3Br_3$-DMSO ink, showing a phase-pure PXRD pattern with a lattice parameter of 10.70 Å and red-shifted absorption and emission spectra with respect to that of the Cs_2TeCl_6 thin film (Figure S11).

Understanding what complexes have been stabilized in these solutions is critical to understanding the ability of these inks to rapidly form phase-pure perovskite structures in ambient conditions. The Te L_3-edge X-ray absorption near edge structure (XANES) of the Cs_2TeBr_6-DMSO ink is measured to probe the coordination environment of Te in solution. XANES is a powerful technique to determine the structural geometry of a dynamic or disordered system such as the inks.[42] Different coordination environments around the Te-center affect its energy transition probed through XANES. For example, a strong white line feature has previously been associated with an electron excitation to the E_g molecular orbital in $[PtCl_6]^{2-}$ octahedral complexes measured in Cs_2PtCl_6 powders.[43] Comparison of the Cs_2TeBr_6-DMSO ink to the Cs_2TeBr_6 powder standard sample displays a similar white line feature as well as other spectral similarities (Figure 3a). Concretely, both samples display broad features in the 20-60 eV past the edge, which are signatures of octahedral molecular resonances A_{1g}, T_{2g}, and E_g.[43] This

confirms that a large population of $[TeBr_6]^{2-}$ octahedral complex anions are stabilized in this ink, as corroborated by the UV-visible absorption data. Furthermore, the ink spectrum also contains a stronger pre-edge feature than the Cs_2TeBr_6 standard, which indicates the presence of anisotropic complexes. Given the dynamic nature of these inks at room temperature,[35] it is not unreasonable to observe such anisotropy. The presence of lower-coordinated Te-based complexes are likely contributing to this anisotropic feature, which is supported by the presence of the same pre-edge feature in the spectrum of the anisotropic, 4-coordinate TeO_2 powder standard sample[44] (inset in Figure 3a). Indeed, this spectral feature has previously been attributed to the co-existence of 4- and 6-coordinate complexes.[45,46] Thus, spectral analysis suggests the presence of both 6-coordinate $[TeBr_6]^{2-}$ and 4-coordinate $[TeBr_4]$ complexes stabilized in the Cs_2TeBr_6-DMSO ink. Similar mixtures of coordination are observed in the XANES analysis of the Cs_2TeCl_6-DMSO and Cs_2TeI_6-DMF inks (Figure S12).

Multiple local coordination environments are also suggested from solution Raman analysis. The solution Raman spectrum of the Cs_2TeBr_6-DMSO ink reveals 4 bands at frequencies 76 cm^{-1}, 147 cm^{-1}, 167 cm^{-1}, and 185 cm^{-1}, which can be assigned to the complexes stabilized in solution (Figure 3b and Figure S13). When compared with the Raman spectrum of the Cs_2TeBr_6 powder, which possesses O_h symmetry, the Cs_2TeBr_6-DMSO ink has vibrational frequencies in the range expected for Te–Br bonds in octahedral or lower-coordinated complexes (approximate Te–Br bond length of 2.70 Å). However, the solid-state Raman spectrum only contains 3 modes corresponding to its O_h symmetry, whereas the solution Raman spectrum contains 4 modes. This indicates that the coordination environment in the inks is not just pure O_h symmetry. Given the UV-visible absorption and XANES analysis, it is possible that 3 of the 4 bands represent the 3 vibrational energies of O_h-symmetric octahedral molecular complexes and

that the fourth band represents a vibrational energy of lower-coordinate molecular complexes. Under this assumption, given the relative frequency positions and intensities of modes in the ink, it is likely that the three lowest frequency modes at 76 cm^{-1}, 147 cm^{-1}, and 167 cm^{-1} correspond to the solvated O_h symmetry units. From this, we can tentatively assign the symmetric stretching A_{1g} mode at 167 cm^{-1}, the asymmetric stretching E_g mode at 147 cm^{-1}, and the bending T_{2g} mode at 76 cm^{-1}. The shifting of the solution modes to slightly lower frequency values compared to the solid-state modes indicates a slight structural relaxation of the Te–Br bond length in the solution-phase.[47] Consequently, the band at 185 cm^{-1} can be tentatively assigned to the solvated 4- or 5-coordinate symmetry units. Since the frequencies for modes resulting from 4-, 5-, and 6-coordinate Te–Br complexes would be quite similar, as confirmed by Raman simulation within a solvent model for the Cs_2TeBr_6-DMSO ink (Figure 3b and Figure S14), this fourth band cannot be definitively assigned to only 4-coordinate [$TeBr_4$] or only 5-coordinate $[TeBr_5]^{1-}$ units. The other bands corresponding to 4- and 5-coordinate vibrating units[48] are likely masked by the increased linewidth of the O_h-symmetric modes brought about by the liquid-phase.[49] Given these mode assignments, quantitative metrics such as integrated peak areas can be used to understand the relative populations of oscillators in solution. The integrated areas for the O_h-symmetric modes ($\int A_{1g}$ = 44457.5, $\int E_g$ = 36659.6, $\int T_{2g}$ = 75537) are an order of magnitude larger than that of the 4-/5-coordinate mode at 185 cm^{-1} ($\int \nu_{4/5}$ = 7985.87), indicating a dominant population of $[TeBr_6]^{2-}$ species in the ink.

As another probe of the complexes stabilized in solution, the Cs_2TeBr_6-DMSO ink is measured using electrospray ionization mass spectrometry (ESI-MS). As shown in Figure 3c, there is a larger population of smaller 4- and 5-coordinate complexes than expected from the UV-visible absorption, XANES, and Raman spectra. This indicates the fragmentation of a large

percentage of the octahedral $[TeBr_6]^{2-}$ complexes during the measurement. This behavior has been observed previously in ESI-MS studies of solvated octahedral complexes, where lower-coordinated complexes are observed instead of the octahedral equivalents.[50,51] However, in the case of the Cs_2TeBr_6-DMSO ink, a small fraction of $[TeBr_6]^{2-}$ complexes are still observed to fly with Cs^+ cations (m/z = 740.3149). The other clusters of peaks have been identified as $[TeBr_5]^{1-}$ at m/z = 528.4964, $[TeBr_4OH]^{1-}$ at m/z = 466.5800, and $[TeBr_3O]^{1-}$ at m/z = 384.6549 via isotope simulation. Similar behavior is observed in both the Raman and ESI-MS spectra of the Cs_2TeCl_6-DMSO and Cs_2TeI_6-DMF inks (Figure S15 and Figure S16).

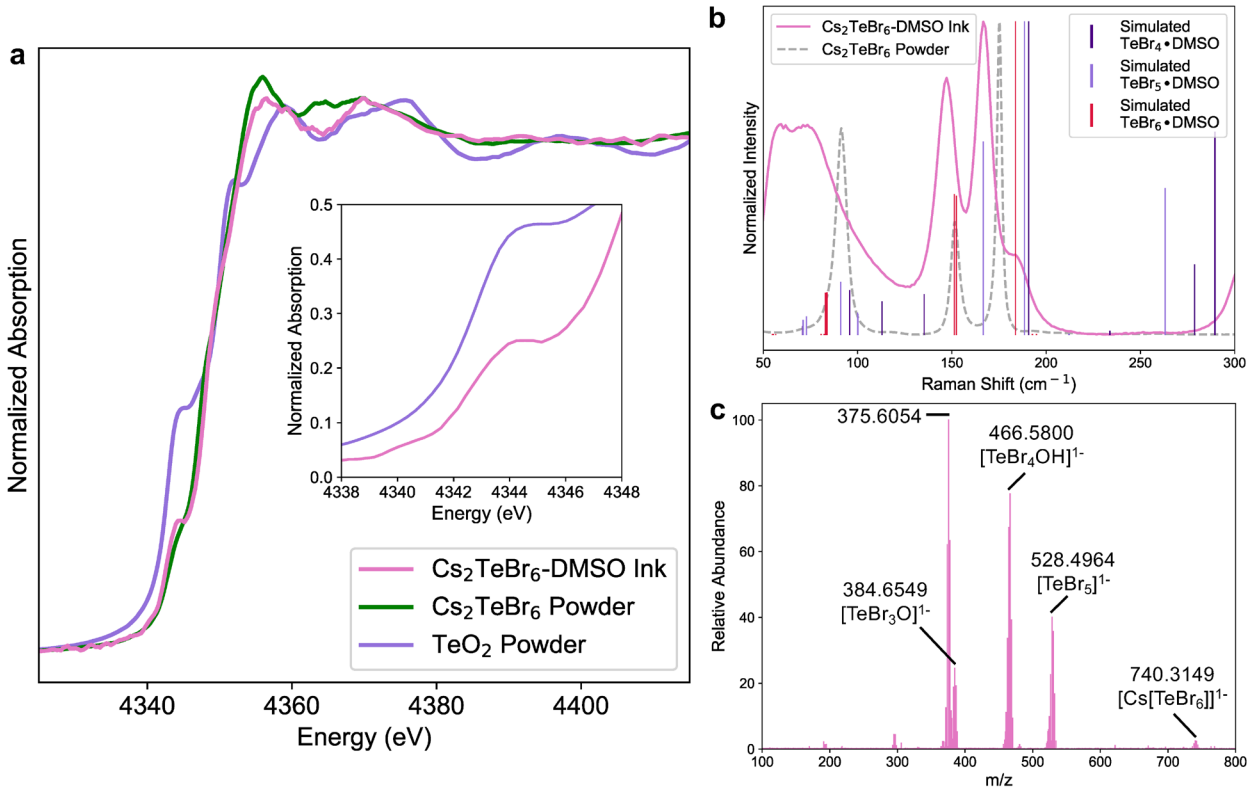

Figure 3. Probing the local coordination environment of the complexes in the inks. (a) The Te L_3-edge X-ray absorption near edge structure (XANES) of the Cs_2TeBr_6-DMSO ink. The ink spectrum has similar features to the Cs_2TeBr_6 powder and TeO_2 powder standards, thus suggesting

the presence of 6-coordinate $[TeBr_6]^{2-}$ and 4-coordinate $[TeBr_4]$ complexes stabilized in solution, respectively. Inset shows the same strong pre-edge feature present in the ink and in the TeO_2 powder. (b) Raman spectrum of the Cs_2TeBr_6-DMSO ink, as compared with that of Cs_2TeBr_6 powder and simulated Raman spectra of 4-, 5-, and 6-coordinate Te–Br complexes in a solvent model. (c) Electrospray ionization mass spectrometry (ESI-MS) spectrum of the Cs_2TeBr_6-DMSO ink.

From structural and spectroscopic evidence, we have designed a ligand-free perovskite semiconductor ink with a majority population of $[TeX_6]^{2-}$ octahedral building blocks stabilized in solution. The unique crystal structure of Cs_2TeX_6 perovskites, with $[TeX_6]^{2-}$ octahedra separated by vacancies, lends itself to facile processability. Starting from the bulk crystal, in which isolated $[TeX_6]^{2-}$ octahedra are stabilized and are charge-balanced by their ionic bonding with Cs^+ cations, the role of the polar solvent is to break this ionic bonding, thus leaving the constituent ionic building blocks stabilized in solution. The control of the ionic bonding allows for the reversible phase transition between the liquid inks and solid-phase perovskite crystals, which is realized through various applications of one-step patterning. More critical than this manipulation of ionic interactions is the stabilization of the $[TeX_6]^{2-}$ octahedral anionic molecules, as these molecules appear to be the key to the rapid formation of phase-pure perovskite structures in ambient conditions. This rational design could therefore be generally applied to other A_2BX_6 systems ($A = K^+, Rb^+, Cs^+$; $B = Te^{4+}, Sn^{4+}, Pd^{4+}, Pt^{4+}, Ti^{4+}, Zr^{4+}$, etc.; $X = Cl^-, Br^-, I^-$), when the bulk A_2BX_6 semiconductor is used as the starting point of ink formation. We have verified this general approach here through tunability in the X-site anion with the formation of mixed-halide $Cs_2TeCl_{6-x}Br_x$ and $Cs_2TeBr_{6-x}I_x$ (x = 0-6) inks, and we are currently exploring tunability in the B-

site cation with the formation of mixed-cation $x\%Te^{4+}:Cs_2SnCl_6$ (x = 0, 1, 2, 5, 10, 20, 35, 50, 75, 100) inks. Starting from the respective emissive bulk $x\%Te^{4+}:Cs_2SnCl_6$ powders (Figure S17), phase-pure inks can be achieved using similar methods to those for the Cs_2TeX_6 inks (Figure S18). The bulk powder approach removes the strong Lewis acid-base interaction between $SnCl_4$/$SnBr_4$ and DMSO/DMF and allows for dissolution of the Sn compounds in these solvents. This is a promising result for future ink formation, as many transition metals that can assume a tetravalent oxidation state are often not naturally occurring in that state.[52,53] Therefore, processable inks can be achieved for any A_2BX_6 system by utilizing our elegant design of dissolving their bulk ionic lattice.

ASSOCIATED CONTENT

Supporting Information

The Supporting Information is available free of charge.

Description of experimental methods and materials characterization; Figures S1−S13 including PXRD patterns, SEM images, UV-visible absorption spectra, experimental and simulated Raman spectra, examples of the geometry-optimized molecules used for simulating Raman modes, XANES spectrum of the Cs_2TeCl_6-DMSO ink, ESI-MS spectrum of the Cs_2TeCl_6-DMSO ink, and other ink compositions realized by our design. (PDF)

AUTHOR INFORMATION

Corresponding Author

***** Email: p_yang@berkeley.edu

ORCID

Maria C. Folgueras – 0000-0001-6502-7616

Sheena Louisia – 0000-0002-2175-6769

Jianbo Jin – 0000-0002-9054-7960

Mengyu Gao – 0000-0003-1385-7364

Alexandra Du – 0000-0002-8712-0835

Peidong Yang – 0000-0003-4799-1684

Author Contributions

The manuscript was written through contributions of all authors. All authors have given approval to the final version of the manuscript.

Notes

The authors declare no competing financial interest.

ACKNOWLEDGEMENT

The authors thank Zhongrui Zhou for assistance in collecting electrospray ionization mass spectrometry measurements, and Marcin Walkiewicz, Dante Zakhidov, and Kirstin Schauble for helpful Raman discussions. This work was financially supported by the BASF CARA program (no. 047010). This research used resources (XFM beamline 10.3.2) of the Advanced Light Source (ALS), a U.S. DOE Office of Science User Facility at Lawrence Berkeley National Laboratory (LBNL) under contract no. DE-AC02-05CH11231. Ultra-low-frequency Raman spectroscopy was performed at the Stanford Nano Shared Facilities (SNSF), and solution Raman

spectroscopy was performed in the Soft and Hybrid Materials Facility (SMF) at SNSF, both supported by the National Science Foundation under award ECCS-2026822. Electrospray ionization mass spectrometry was performed at the UC Berkeley QB3/Chemistry Mass Spectrometry Facility. Scanning electron microscopy was conducted at the UC Berkeley QB3 Biomolecular Nanotechnology Center (BNC). J.J. acknowledges fellowship support from Suzhou Industrial Park.

REFERENCES

(1) Farid, B.; Godby, R. W. Cohesive Energies of Crystals. *Phys. Rev. B* **1991**, *43* (17), 14248–14250. https://doi.org/10.1103/PhysRevB.43.14248.

(2) Zhou, W.; Zhong, X.; Sheng, K. High Temperature Stability Evaluation of SiC MOSFETs. In *2014 IEEE 26th International Symposium on Power Semiconductor Devices & IC's (ISPSD)*; IEEE, 2014; Vol. 29, pp 305–308. https://doi.org/10.1109/ISPSD.2014.6856037.

(3) Assad, F.; Zhibin Ren; Vasileska, D.; Datta, S.; Lundstrom, M. On the Performance Limits for Si MOSFETs: A Theoretical Study. *IEEE Trans. Electron Devices* **2000**, *47* (1), 232–240. https://doi.org/10.1109/16.817590.

(4) Yamamoto, K.; Yoshikawa, K.; Uzu, H.; Adachi, D. High-Efficiency Heterojunction Crystalline Si Solar Cells. *Jpn. J. Appl. Phys.* **2018**, *57* (8S3), 08RB20. https://doi.org/10.7567/JJAP.57.08RB20.

(5) Stern, F. Gain-Current Relation for GaAs Lasers with n-Type and Undoped Active Layers. *IEEE J. Quantum Electron.* **1973**, *9* (2), 290–294. https://doi.org/10.1109/JQE.1973.1077478.

(6) Shimura, F. Single-Crystal Silicon: Growth and Properties. In *Springer Handbook of Electronic and Photonic Materials*; Kasap, S., Capper, P., Eds.; Springer International Publishing: Cham, 2017; pp 293–307. https://doi.org/10.1007/978-3-319-48933-9_13.

(7) Orr, B. G. An STM Study of Molecular-Beam Epitaxy Growth of GaAs. *J. Cryst. Growth* **1993**, *127* (1–4), 247–257. https://doi.org/10.1016/0022-0248(93)90784-T.

(8) Mitzi, D. B. Solution-Processed Inorganic Semiconductors. *J. Mater. Chem.* **2004**, *14* (15), 2355–2365. https://doi.org/10.1039/b403482a.

(9) Murray, C. B.; Norris, D. J.; Bawendi, M. G. Synthesis and Characterization of Nearly Monodisperse CdE (E = Sulfur, Selenium, Tellurium) Semiconductor Nanocrystallites. *J. Am. Chem. Soc.* **1993**, *115* (19), 8706–8715. https://doi.org/10.1021/ja00072a025.

(10) Wang, Y.; Fedin, I.; Zhang, H.; Talapin, D. V. Direct Optical Lithography of Functional Inorganic Nanomaterials. *Science* **2017**, *357* (6349), 385–388. https://doi.org/10.1126/science.aan2958.

(11) Lee, K. S.; Blanchet, G. B.; Gao, F.; Loo, Y.-L. Direct Patterning of Conductive Water-Soluble Polyaniline for Thin-Film Organic Electronics. *Appl. Phys. Lett.* **2005**, *86* (7), 074102. https://doi.org/10.1063/1.1862345.

(12) Palma, C.-A.; Samorì, P. Blueprinting Macromolecular Electronics. *Nat. Chem.* **2011**, *3* (6), 431–436. https://doi.org/10.1038/nchem.1043.

(13) Anthopoulos, T. D.; Tanase, C.; Setayesh, S.; Meijer, E. J.; Hummelen, J. C.; Blom, P. W. M.; de Leeuw, D. M. Ambipolar Organic Field-Effect Transistors Based on a Solution-Processed Methanofullerene. *Adv. Mater.* **2004**, *16* (23–24), 2174–2179. https://doi.org/10.1002/adma.200400309.

(14) Kovalenko, M. V.; Protesescu, L.; Bodnarchuk, M. I. Properties and Potential

Optoelectronic Applications of Lead Halide Perovskite Nanocrystals. *Science* **2017**, *358* (6364), 745–750. https://doi.org/10.1126/science.aam7093.

(15) Quan, L. N.; García de Arquer, F. P.; Sabatini, R. P.; Sargent, E. H. Perovskites for Light Emission. *Adv. Mater.* **2018**, *30* (45), 1801996. https://doi.org/10.1002/adma.201801996.

(16) Swarnkar, A.; Marshall, A. R.; Sanehira, E. M.; Chernomordik, B. D.; Moore, D. T.; Christians, J. A.; Chakrabarti, T.; Luther, J. M. Quantum Dot-Induced Phase Stabilization of a-$CsPbI_3$ Perovskite for High-Efficiency Photovoltaics. *Science* **2016**, *354* (6308), 92–95. https://doi.org/10.1126/science.aag2700.

(17) Liang, J.; Wang, C.; Wang, Y.; Xu, Z.; Lu, Z.; Ma, Y.; Zhu, H.; Hu, Y.; Xiao, C.; Yi, X.; Zhu, G.; Lv, H.; Ma, L.; Chen, T.; Tie, Z.; Jin, Z.; Liu, J. All-Inorganic Perovskite Solar Cells. *J. Am. Chem. Soc.* **2016**, *138* (49), 15829–15832. https://doi.org/10.1021/jacs.6b10227.

(18) Quan, L. N.; Kang, J.; Ning, C.-Z.; Yang, P. Nanowires for Photonics. *Chem. Rev.* **2019**, *119* (15), 9153–9169. https://doi.org/10.1021/acs.chemrev.9b00240.

(19) Kim, Y.-H.; Kim, S.; Kakekhani, A.; Park, J.; Park, J.; Lee, Y.-H.; Xu, H.; Nagane, S.; Wexler, R. B.; Kim, D.-H.; Jo, S. H.; Martínez-Sarti, L.; Tan, P.; Sadhanala, A.; Park, G.-S.; Kim, Y.-W.; Hu, B.; Bolink, H. J.; Yoo, S.; Friend, R. H.; Rappe, A. M.; Lee, T.-W. Comprehensive Defect Suppression in Perovskite Nanocrystals for High-Efficiency Light-Emitting Diodes. *Nat. Photonics* **2021**, *15* (2), 148–155. https://doi.org/10.1038/s41566-020-00732-4.

(20) Wang, Y.; Yuan, F.; Dong, Y.; Li, J.; Johnston, A.; Chen, B.; Saidaminov, M. I.; Zhou, C.; Zheng, X.; Hou, Y.; Bertens, K.; Ebe, H.; Ma, D.; Deng, Z.; Yuan, S.; Chen, R.; Sagar, L. K.; Liu, J.; Fan, J.; Li, P.; Li, X.; Gao, Y.; Fung, M.; Lu, Z.; Bakr, O. M.; Liao, L.;

Sargent, E. H. All-Inorganic Quantum-Dot LEDs Based on a Phase-Stabilized A-$CsPbI_3$ Perovskite. *Angew. Chemie Int. Ed.* **2021**, *60* (29), 16164–16170. https://doi.org/10.1002/anie.202104812.

(21) Song, J.; Cui, Q.; Li, J.; Xu, J.; Wang, Y.; Xu, L.; Xue, J.; Dong, Y.; Tian, T.; Sun, H.; Zeng, H. Ultralarge All-Inorganic Perovskite Bulk Single Crystal for High-Performance Visible-Infrared Dual-Modal Photodetectors. *Adv. Opt. Mater.* **2017**, *5* (12), 1700157. https://doi.org/10.1002/adom.201700157.

(22) Glushkova, A.; Andričević, P.; Smajda, R.; Náfrádi, B.; Kollár, M.; Djokić, V.; Arakcheeva, A.; Forró, L.; Pugin, R.; Horváth, E. Ultrasensitive 3D Aerosol-Jet-Printed Perovskite X-Ray Photodetector. *ACS Nano* **2021**, *15* (3), 4077–4084. https://doi.org/10.1021/acsnano.0c07993.

(23) Mishra, S.; Ghosh, S.; Singh, T. Progress in Materials Development for Flexible Perovskite Solar Cells and Future Prospects. *ChemSusChem* **2021**, *14* (2), 512–538. https://doi.org/10.1002/cssc.202002095.

(24) Hui, W.; Chao, L.; Lu, H.; Xia, F.; Wei, Q.; Su, Z.; Niu, T.; Tao, L.; Du, B.; Li, D.; Wang, Y.; Dong, H.; Zuo, S.; Li, B.; Shi, W.; Ran, X.; Li, P.; Zhang, H.; Wu, Z.; Ran, C.; Song, L.; Xing, G.; Gao, X.; Zhang, J.; Xia, Y.; Chen, Y.; Huang, W. Stabilizing Black-Phase Formamidinium Perovskite Formation at Room Temperature and High Humidity. *Science* **2021**, *371* (6536), 1359–1364. https://doi.org/10.1126/science.abf7652.

(25) Wei, Z.; Chen, H.; Yan, K.; Yang, S. Inkjet Printing and Instant Chemical Transformation of a $CH_3NH_3PbI_3$/Nanocarbon Electrode and Interface for Planar Perovskite Solar Cells. *Angew. Chemie Int. Ed.* **2014**, *53* (48), 13239–13243. https://doi.org/10.1002/anie.201408638.

(26) Mathies, F.; Abzieher, T.; Hochstuhl, A.; Glaser, K.; Colsmann, A.; Paetzold, U. W.; Hernandez-Sosa, G.; Lemmer, U.; Quintilla, A. Multipass Inkjet Printed Planar Methylammonium Lead Iodide Perovskite Solar Cells. *J. Mater. Chem. A* **2016**, *4* (48), 19207–19213. https://doi.org/10.1039/C6TA07972E.

(27) Li, S.-G.; Jiang, K.-J.; Su, M.-J.; Cui, X.-P.; Huang, J.-H.; Zhang, Q.-Q.; Zhou, X.-Q.; Yang, L.-M.; Song, Y.-L. Inkjet Printing of $CH_3NH_3PbI_3$ on a Mesoscopic TiO_2 Film for Highly Efficient Perovskite Solar Cells. *J. Mater. Chem. A* **2015**, *3* (17), 9092–9097. https://doi.org/10.1039/C4TA05675B.

(28) Li, Z.; Yang, M.; Park, J.-S.; Wei, S.-H.; Berry, J. J.; Zhu, K. Stabilizing Perovskite Structures by Tuning Tolerance Factor: Formation of Formamidinium and Cesium Lead Iodide Solid-State Alloys. *Chem. Mater.* **2016**, *28* (1), 284–292. https://doi.org/10.1021/acs.chemmater.5b04107.

(29) Li, S.; Xu, X.-L.; Yang, Y.; Xu, Y.-S.; Xu, Y.; Xia, H. Highly Deformable High-Performance Paper-Based Perovskite Photodetector with Improved Stability. *ACS Appl. Mater. Interfaces* **2021**, *13* (27), 31919–31927. https://doi.org/10.1021/acsami.1c05828.

(30) Steele, J. A.; Jin, H.; Dovgaliuk, I.; Berger, R. F.; Braeckevelt, T.; Yuan, H.; Martin, C.; Solano, E.; Lejaeghere, K.; Rogge, S. M. J.; Notebaert, C.; Vandezande, W.; Janssen, K. P. F.; Goderis, B.; Debroye, E.; Wang, Y.-K.; Dong, Y.; Ma, D.; Saidaminov, M.; Tan, H.; Lu, Z.; Dyadkin, V.; Chernyshov, D.; Van Speybroeck, V.; Sargent, E. H.; Hofkens, J.; Roeffaers, M. B. J. Thermal Unequilibrium of Strained Black $CsPbI_3$ Thin Films. *Science* **2019**, *365* (6454), 679–684. https://doi.org/10.1126/science.aax3878.

(31) Chen, M.; Ju, M.-G.; Garces, H. F.; Carl, A. D.; Ono, L. K.; Hawash, Z.; Zhang, Y.; Shen, T.; Qi, Y.; Grimm, R. L.; Pacifici, D.; Zeng, X. C.; Zhou, Y.; Padture, N. P. Highly Stable

and Efficient All-Inorganic Lead-Free Perovskite Solar Cells with Native-Oxide Passivation. *Nat. Commun.* **2019**, *10* (1), 16. https://doi.org/10.1038/s41467-018-07951-y.

(32) Kazes, M.; Udayabhaskararao, T.; Dey, S.; Oron, D. Effect of Surface Ligands in Perovskite Nanocrystals: Extending in and Reaching Out. *Acc. Chem. Res.* **2021**, *54* (6), 1409–1418. https://doi.org/10.1021/acs.accounts.0c00712.

(33) Jin, J.; Folgueras, M. C.; Gao, M.; Yu, S.; Louisia, S.; Zhang, Y.; Quan, L. N.; Chen, C.; Zhang, R.; Seeler, F.; Schierle-Arndt, K.; Yang, P. A New Perspective and Design Principle for Halide Perovskites: Ionic Octahedron Network (ION). *Nano Lett.* **2021**, *21* (12), 5415–5421. https://doi.org/10.1021/acs.nanolett.1c01897.

(34) Couch, D. A.; Wilkins, C. J.; Rossman, G. R.; Gray, H. B. Electronic Energy Levels in Hexahalotellurate(IV) Complexes. *J. Am. Chem. Soc.* **1970**, *92* (2), 307–310. https://doi.org/10.1021/ja00705a014.

(35) Stufkens, D. J. Dynamic Jahn-Teller Effect in the Excited States of $SeCl_6^{2-}$, $SeBr_6^{2-}$, $TeCl_6^{2-}$ and $TeBr_6^{2-}$: Interpretation of Electronic Absorption and Raman Spectra. *Recl. des Trav. Chim. des Pays-Bas* **1970**, *89* (11), 1185–1201. https://doi.org/10.1002/recl.19700891109.

(36) Sun, Q.; Qu, B.; Shi, J. Investigation of Relations between Absorption Band Positions and Crystalline Environment in Pb2+-Doped Alkali Halides. *Phys. Chem. Chem. Phys.* **2010**, *12* (16), 4178–4183. https://doi.org/10.1039/b921791f.

(37) Dunlap-Shohl, W. A.; Zhou, Y.; Padture, N. P.; Mitzi, D. B. Synthetic Approaches for Halide Perovskite Thin Films. *Chem. Rev.* **2019**, *119* (5), 3193–3295. https://doi.org/10.1021/acs.chemrev.8b00318.

(38) Vázquez-Fernández, I.; Mariotti, S.; Hutter, O. S.; Birkett, M.; Veal, T. D.; Hobson, T. D.

C.; Phillips, L. J.; Danos, L.; Nayak, P. K.; Snaith, H. J.; Xie, W.; Sherburne, M. P.; Asta, M.; Durose, K. Vacancy-Ordered Double Perovskite Cs2TeI6 Thin Films for Optoelectronics. *Chem. Mater.* **2020**, *32* (15), 6676–6684. https://doi.org/10.1021/acs.chemmater.0c02150.

(39) Sedakova, T. V.; Mirochnik, A. G.; Karasev, V. E. Structure and Luminescence Properties of Tellurium(IV) Complex Compounds. *Opt. Spectrosc.* **2011**, *110* (5), 755–761. https://doi.org/10.1134/S0030400X11030192.

(40) McCall, K. M.; Morad, V.; Benin, B. M.; Kovalenko, M. V. Efficient Lone-Pair-Driven Luminescence: Structure–Property Relationships in Emissive $5s^2$ Metal Halides. *ACS Mater. Lett.* **2020**, *2* (9), 1218–1232. https://doi.org/10.1021/acsmaterialslett.0c00211.

(41) Benin, B. M.; Dirin, D. N.; Morad, V.; Wörle, M.; Yakunin, S.; Rainò, G.; Nazarenko, O.; Fischer, M.; Infante, I.; Kovalenko, M. V. Highly Emissive Self-Trapped Excitons in Fully Inorganic Zero-Dimensional Tin Halides. *Angew. Chemie Int. Ed.* **2018**, *57* (35), 11329–11333. https://doi.org/10.1002/anie.201806452.

(42) D'Angelo, P.; Migliorati, V. Solvation Structure of Zn^{2+} and Cu^{2+} Ions in Acetonitrile: A Combined EXAFS and XANES Study. *J. Phys. Chem. B* **2015**, *119* (10), 4061–4067. https://doi.org/10.1021/acs.jpcb.5b01634.

(43) Nemanova, V. I.; Kondratenko, A. V.; Ruzankin, S. F.; Bausk, N. V.; Zhidomirov, G. M.; Mazalov, L. N. Xanes of the Pd and Pt Atoms in Square and Octahedral Chloride Complexes. *Chem. Phys.* **1987**, *116* (1), 61–68. https://doi.org/10.1016/0301-0104(87)80068-X.

(44) Marple, M. A. T.; Jesuit, M.; Hung, I.; Gan, Z.; Feller, S.; Sen, S. Structure of TeO_2 Glass: Results from 2D ^{125}Te NMR Spectroscopy. *J. Non. Cryst. Solids* **2019**, *513* (March), 183–

190. https://doi.org/10.1016/j.jnoncrysol.2019.03.019.

(45) Belli, M.; Scafati, A.; Bianconi, A.; Mobilio, S.; Palladino, L.; Reale, A.; Burattini, E. X-Ray Absorption near Edge Structures (XANES) in Simple and Complex Mn Compounds. *Solid State Commun.* **1980**, *35* (4), 355–361. https://doi.org/10.1016/0038-1098(80)90515-3.

(46) Asakura, K.; Nomura, M.; Kuroda, H. Fe K-Edge XANES and EXAFS of the X-Ray Absorption Spectra of $FeCl_3$ Aqueous Solutions. A Structural Study of the Solute, Iron(III) Chloro Complexes. *Bull. Chem. Soc. Jpn.* **1985**, *58* (5), 1543–1550. https://doi.org/10.1246/bcsj.58.1543.

(47) Nims, C.; Cron, B.; Wetherington, M.; Macalady, J.; Cosmidis, J. Low Frequency Raman Spectroscopy for Micron-Scale and in Vivo Characterization of Elemental Sulfur in Microbial Samples. *Sci. Rep.* **2019**, *9* (1), 7971. https://doi.org/10.1038/s41598-019-44353-6.

(48) Ponsioen, R.; Stufkens, D. J. The Raman and Infrared Spectra of Solid $TeCl_4$ AND $SeCl_4$. *Recl. des Trav. Chim. des Pays-Bas* **1971**, *90* (5), 521–528. https://doi.org/10.1002/recl.19710900508.

(49) Zhu, G.; Zhu, X.; Fan, Q.; Wan, X. Raman Spectra of Amino Acids and Their Aqueous Solutions. *Spectrochim. Acta Part A Mol. Biomol. Spectrosc.* **2011**, *78* (3), 1187–1195. https://doi.org/10.1016/j.saa.2010.12.079.

(50) Allen, C. S.; Chuang, C.-L.; Cornebise, M.; Canary, J. W. Electrospray Mass Spectrometry and X-Ray Crystallography Studies of Divalent Metal Ion Complexes of Tris(2-Pyridylmethyl) Amine. *Inorganica Chim. Acta* **1995**, *239* (1–2), 29–37. https://doi.org/10.1016/0020-1693(95)04710-7.

(51) Valle, G.; Ettorre, R.; Vettori, U.; Peruzzo, V.; Plazzogna, G. Crystal Structure and Mass Spectrometry of Dichlorodimethylbis[2(1H)-Pyridinethione-S]Tin(IV). *J. Chem. Soc. Dalt. Trans.* **1987**, *2* (4), 815–817. https://doi.org/10.1039/dt9870000815.

(52) Sakai, N.; Haghighirad, A. A.; Filip, M. R.; Nayak, P. K.; Nayak, S.; Ramadan, A.; Wang, Z.; Giustino, F.; Snaith, H. J. Solution-Processed Cesium Hexabromopalladate(IV), Cs_2PdBr_6, for Optoelectronic Applications. *J. Am. Chem. Soc.* **2017**, *139* (17), 6030–6033. https://doi.org/10.1021/jacs.6b13258.

(53) Yang, S.; Wang, L.; Zhao, S.; Liu, A.; Zhou, Y.; Han, Q.; Yu, F.; Gao, L.; Zhang, C.; Ma, T. Novel Lead-Free Material Cs_2PtI_6 with Narrow Bandgap and Ultra-Stability for Its Photovoltaic Application. *ACS Appl. Mater. Interfaces* **2020**, *12* (40), 44700–44709. https://doi.org/10.1021/acsami.0c11429.

TABLE OF CONTENTS GRAPHIC